Structure transitions in oblate nematic droplets

V. Yu. Rudyak,[1,*] A. V. Emelyanenko,[1] and V. A. Loiko[2]
[1]*Department of Physics, M.V. Lomonosov Moscow State University, Moscow, 119991, Russia*
[2]*B.I. Stepanov Institute of Physics of the National Academy of Sciences of Belarus, Nezalezhnasti Avenue 68, Minsk 220072, Belarus*
(Received 18 June 2013; revised manuscript received 1 October 2013; published 13 November 2013)

We consider the structure transitions in oblate supramicrometer nematic droplets related to reorientation of the line defect in the electric field. These transitions can be used in optical devices based on polymer dispersed liquid crystal materials with high contrast ratio. We suggest a simple method for determination of director distribution in nematic droplets of an arbitrary shape with surface interaction and in the presence of constant electric field. Point and linear defects are taken into account. This method does not require any presuppositions about symmetry of the director distribution. The elasticity continuum theory is treated with Monte Carlo annealing on a simple lattice. A special triangulation-based technique is applied for accurate representation of the droplet boundaries. The method is tested on 5CB material.

DOI: 10.1103/PhysRevE.88.052501 PACS number(s): 61.30.Jf, 64.70.M−, 61.30.Pq, 61.30.Cz

I. INTRODUCTION

Polymer dispersed liquid crystals (PDLC) [1–6] are known for their ability to combine the properties of polymers (including the ability to form flexible films and coatings) with the unique properties of liquid crystals capable of orientation during the action of a weak external field and changes in optical characteristics (transparency, birefringence, light scattering, etc.). They are usually prepared in the form of microdroplets dispersed in a polymer matrix. An important feature of PDLC materials is their adjustable optical properties, including refractive indices [7,8]. For example, under electric field the initially nontransparent PDLC material can become optically transparent. The application of PDLC films can be very wide: electrically controlled blinds, fast-acting optical attenuators, large-sized display boards, for example, as well as controlled road signs, petrol pump indicators, railway station and airport information boards, etc. Since PDLC materials do not require the presence of polarizers, they are also convenient for the construction of small and flexible optical devices [9,10]. Prediction of the material properties (optical, electro-optical, elastic, etc.) is one of the most important practical targets.

At the moment it is already possible to predict the order parameters and elasticity constants in uniform materials from the properties of single molecules constituting liquid crystals (geometry and interactions) [11,12]. There are a few publications [13], where distribution of the director in the nematic droplet is predicted theoretically. At the same time, there is only little success in the theoretical prediction of the director distribution in confined systems, particularly in droplets of complex surface boundaries.

In this case computer simulation methods can be very helpful. One of the simplest approaches for nematics is the Lebwohl-Lasher lattice model [14] usually simulated by the Monte Carlo (MC) method. This approach is very fast due to simplicity of the model, although it cannot be applicable to distorted nematic structures. For a more detailed description, two different approaches were used. Yao *et al*. [15,16] suggested a finite element method based approach to the Frank-Oseen free energy formulation using a vectorial representation of director field. However, the complexity of the system required an iterative solution of the problem starting from a reasonable initial condition. Even with these limitations, the method was able to solve two-dimensional systems only. Another approach is the Landau–de Gennes model [17–19] which is also usually treated with a finite element method and explicit relaxation algorithms [20,21]. This method is very good in reproducing a detailed structure with defects of various types, and is more precise than director-based ones. However, the major disadvantage of this approach is its high computational cost.

Meanwhile, there are many tasks requiring fast investigation of a liquid crystal structure in a large set of various conditions (i.e., a large set of calculational tasks is required), with no need of fine details. Therefore it is very important to have a fast method predicting structure of a droplet with a minimal set of input data.

In the present paper we suggest a method based on the elasticity continuum theory [22] applied numerically to director distribution on a simple lattice. This approach is generally similar to the one suggested in [15], but with three major differences. First, we use the Monte Carlo method with simulated annealing [23] for the free energy optimization. This procedure does not require any physically reasonable initial state, fast enough and easily parallelizable. Secondly, we included linear and point defects in an explicit description of the system, and thus, we use a much more general approach. Thirdly, we introduce a triangulation technique to represent boundaries that allow one to study a system with any given shape.

Our approach is capable of predicting the structures of nematic droplets of complex geometries, where the director distribution and the shape of defects cannot be presupposed from symmetry arguments. In this paper we consider the oblate supramicrometer nematic droplets. PDLC materials containing oblate droplets are highly attractive for a set of applications, including reflecting flat panel displays [24–28], diffraction lenses [29], and other applications [30–34]. While spherical nematic droplets had been exhaustively examined [35–38], including stable structures at various surface anchoring

*vurdizm@gmail.com

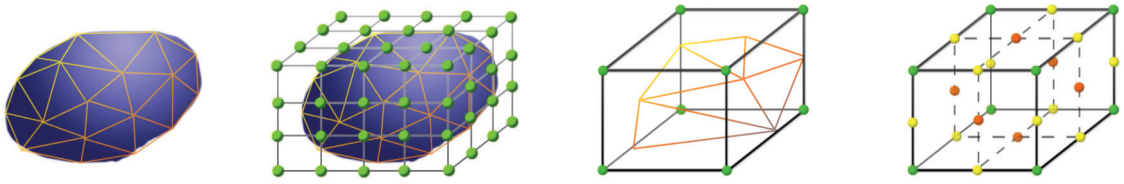

(a) (b) (c) (d)

FIG. 1. (Color online) Schematic representation of the surface triangulation treatment: (a) surface and its triangulation; (b) cubic lattice covering the surface (director vectors are defined in vertices shown as points); (c) retriangulation in a chosen cell; (d) cube vertices and oversampling points: edge middles (yellow dots on intersections of ribs and dashed lines) and facet middles (red dots on intersections of dashed lines).

conditions [39] and phase transitions in the presence of electric field [17,40], oblate droplets are still under active study. These studies show the presence of radial, bipolar, and radial with circular defect structures under various conditions. However, the complete phase diagrams for oblate droplets under electric field were not resolved. The last step towards this task was done in [40], where the systems with negative electric anisotropy were studied. In this paper, we study the behavior of oblate droplets with a positive electric anisotropy factor under electric field.

In particular, we show that the line defect can exist in oblate nematic droplets even without electric field, as was previously displayed in [41]. We have also found out the new phase transition resulting in reorientation of the line defect, when the electric field applied along the plane, to which the line defect belongs, exceeds some critical value. This transition should drastically change the optical properties of PDLC materials composed of oblate droplets, and thus can be used for the creation of optical devices with high contrast ratios. This effect is not observed in PDLC materials composed of conventional spherical droplets.

The paper is organized as follows. In Sec. II we start with a description of the method. In Sec. III the results of computer simulation for nematics in spherical and oblate droplets under electric field will be presented and discussed. Finally, the conclusions will be made in Sec. IV.

II. METHOD

A. Geometry of the system

We consider a finite nematic liquid crystal (LC) with a regular boundary surface. Recent approaches concern only particular analytically described boundary shapes (cube, sphere, set of spheres, set of ellipsoids, etc.). Here we present the method of director distribution calculation in nematic LC droplets of any shape, including channels and cavities inside of a finite volume, using a combination of the triangulation technique and simple cubic lattice.

1. Boundary surface setup

Let us approximate the real border dividing the LC material and surrounding media by a polyhedron consisting of triangles. This procedure, called triangulation, is well known [42] from computer graphics and can be applied to any regular surface *with any desired accuracy*. The triangulated surface (T) can be of any complexity and be obtained from most computer-aided design packages.

2. Space discretization

The next task is to discretize the volume, inside of which director $\mathbf{n}(\bar{r})$ is distributed. We suggest the following algorithm. Let us introduce the rectangular lattice in the larger space than volume inside of T. Then continuous director field $\mathbf{n}(\bar{r})$ is replaced with a set of vectors $\mathbf{n}(\bar{r}_{ijk})$, where i, j, and k are the lattice indexes and $\bar{r}_{ijk}$ are the positions of lattice vertices (bold points in Fig. 1).

The lattice divides the entire volume into rectangular cells (cuboids limited by eight nearest lattice points). All the cells can be divided into three groups: "inside cells," which are fully inside of T, "outside cells" that are fully outside of T, and "surface cells" that are intersecting with T. Finally, retriangulation proceeds for each surface cell, which produces a set of triangles (T_i) belonging to initial surface T and located completely inside of the cell or at its boundaries (see Fig. 1).

B. Free energy representation

In the framework of elasticity continuum theory, free energy of the system F is supposed to be a functional of the director distribution. As the entire volume of the system is divided into rectangular cells, one can write the total free energy of the entire volume as a sum of the free energies of each subvolume:

$$F = \sum_i F^{(i)},$$

where $F^{(i)}$ is the free energy of the ith cell, which is independent of the free energies of the other cells. Each energy $F^{(i)}$ is calculated as a sum of the four terms:

$$F^{(i)} = F^{(i)}_{\text{el}} + F^{(i)}_{S} + F^{(i)}_{\text{ext}} + F^{(i)}_{\text{def}},$$

where $F^{(i)}_{\text{el}}$ is the elasticity energy, $F^{(i)}_{S}$ is the anchoring energy, $F^{(i)}_{\text{ext}}$ is the interaction of LC molecules with the external electric field, and $F^{(i)}_{\text{def}}$ is the energy of defects. The first three terms are usually considered in the framework of continuum theory, while the fourth term, $F^{(i)}_{\text{def}}$, is the additional contribution allowing one to take defects into account. Particular expressions for each term are considered below.

1. Elasticity energy

The Frank elasticity free energy [22] per unit volume of a nematic LC can be written in the following form:

$$f_{\rm el} = \frac{K_{11}}{2}(\mathrm{div}\,\mathbf{n})^2 + \frac{K_{22}}{2}(\mathbf{n}\cdot\mathrm{rot}\,\mathbf{n})^2 + \frac{K_{33}}{2}[\mathbf{n}\times\mathrm{rot}\,\mathbf{n}]^2,$$

where K_{11}, K_{22}, and K_{33} are the splay, twist, and bend elasticity constants. The elasticity energy of each cell $F_{\rm el}^{(i)} = \int_V f_{\rm el}^{(i)}\,dv$ is calculated here as the average $f_{\rm el}^{(i,\alpha)}V_i$ over four of eight vertices, which are enumerated by index α. In these vertices all gradient terms $\frac{\partial \mathbf{n}}{\partial \bar{r}}$ are calculated numerically and then $f_{\rm el}^{(i,\alpha)}$ is calculated explicitly. Here V_i is the volume of the ith cell inside of surface T (which is equal to the volume of the cells' cuboid V_0 for the inside cells, equal to zero for the outside cells, and varies from zero to V_0 for the surface cells).

2. Anchoring energy

We use Rapini-Papoular approximation for the anchoring energy [43]. The total surface anchoring energy is calculated as a sum of the energies of all triangles:

$$F_S = \sum_t \frac{W_t S_t}{2}\begin{cases}(\mathbf{n}_t\cdot\mathbf{a}_t)^2 & \text{planar}\\ 1-(\mathbf{n}_t\cdot\mathbf{a}_t)^2 & \text{homeotropic,}\end{cases}$$

where W_t is the anchoring strength at the tth triangle, S_t is the surface area of the tth triangle, $\mathbf{n}_t$ is the director in the center of the tth triangle, and $\mathbf{a}_t$ denotes the easy axis vector for the tth triangle. Anchoring strength W_t is positive for planar anchoring and negative for homeotropic anchoring.

3. Electric-field energy

Electric-field energy density can be written as follows [44]:

$$f_{\rm ext}^{(i)} = -\varepsilon_0\Delta\varepsilon\,(\mathbf{E}\cdot\mathbf{n})^2,$$

where $\mathbf{E}$ is the electric-field intensity. Any particular distribution of electric field can be taken into account. $\mathbf{E}$ is assumed to be independent of the director field distribution. Integration of $f_{\rm ext}^{(i)}$ over the cell is replaced with the summation over 26 key points at the surface of the cell:

$$F_{\rm ext}^{(i)} = \sum_k v_k\, f_{\rm ext}^{(i)},$$

where v_k is a part of a cell "related" to the kth key point ($v_k = \frac{1}{64}V_i$ for vertices, $\frac{1}{32}V_i$ for edge middles, and $\frac{1}{12}V_i$ for facet middles).

4. Determination of point and linear defects

As mentioned above, it is important to take into account the defects in confined geometries. However, the elastic continuum theory can only describe a small distortion of the director vector field $\mathbf{n}(\bar{r})$. Therefore computer minimization of the free energy based solely on the elastic continuum theory can result in the wrong position and kind of defects. To avoid this mistake, one should be able to identify the defects at particular lattice cells and to replace their free energy following from continuum theory with different values specific to certain kinds of defects. Here we are going to suggest a simple computer algorithm allowing one to identify the positions and kinds of defects. This algorithm is based on the idea that director orientations in different areas adjacent to a defect should be incompatible with each other.

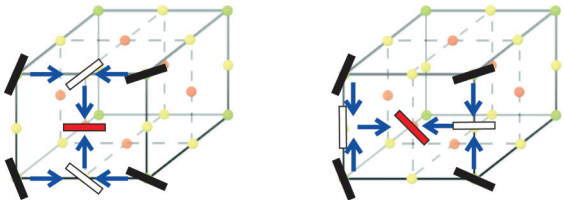

FIG. 2. (Color online) Origin of misalignment. Black bars are the in-lattice director vectors, white bars are the averages in the edge middles obtained at the first step, and red (light gray) bars are the averages in the facet middles obtained at the second step. (a) and (b) represent the two ways of calculating the director in the facet middle leading to different results $\tilde{\mathbf{n}}_1$ and $\tilde{\mathbf{n}}_2$.

An example of the director incompatibility is presented in Fig. 2, where the two ways of calculatiing the director vector in a facet center are shown. In the first way the director is averaged along the horizontal direction first, and then along the vertical direction, while in the second way the director is averaged along the vertical direction first, and then along the horizontal direction. One can see from Fig. 2 that these ways [presented either in Fig. 2(a) or in Fig. 2(b)] lead to different director orientations in the facet centers [red (light gray) bars]. We have empirically found that this difference corresponds to the presence of a defect. As a numerical measure of this difference, let us introduce the *misalignment* for a rectangular facet middle [red dots in Fig. 1(d)] as

$$m_{\rm facet} = 1 - \cos^2(\tilde{\mathbf{n}}_1,\tilde{\mathbf{n}}_2),$$

where $\tilde{\mathbf{n}}_1$ and $\tilde{\mathbf{n}}_2$ are the average directors along two principal dimensions of a facet (white bars in Fig. 2), and for the center of a cubic cell as

$$m_{cp} = 1 - \min\{\cos^2(\tilde{\mathbf{n}}_x,\tilde{\mathbf{n}}_y);\cos^2(\tilde{\mathbf{n}}_x,\tilde{\mathbf{n}}_z);\cos^2(\tilde{\mathbf{n}}_y,\tilde{\mathbf{n}}_z)\},$$

where $\tilde{\mathbf{n}}_x$, $\tilde{\mathbf{n}}_y$, and $\tilde{\mathbf{n}}_z$ are the averages for each pair of opposite facet middles (facets perpendicular to the x, y, and z axes, respectively). The misalignment is expected to be small in the cells with small director distortion, while it is expected to be large in the cells with large director distortion, and therefore can be used for the identification of defects.

Totally we have seven misalignment values for each cell ($m_i = 1,\ldots,7$) (six facet middles and one cell center). Let us introduce the two critical misalignments $m_{\rm min}$ and $m_{\rm max}$, below and above which the defect strength is either considered to be equal to zero (the defect is absent) or equal to one (the defect is present), while between $m_i^{\rm min}$ and $m_i^{\rm max}$ let us consider the defect with some probability (defect strength) approximated by polynomials of the corresponding misalignment:

$$d_i = \sum_n \alpha_n m_i^n,$$

where it is enough to consider the four terms to spline the probability between zero for $m_i = m_{\rm min}$ and one for $m_i = m_{\rm max}$ with gradient growth in between (see Fig. 3).

In addition, it is critically important to distinguish the point and linear defects. For this purpose, let us introduce the segment defect strength for each of six segments connecting

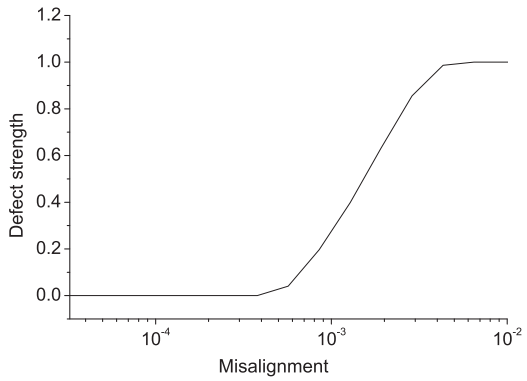

FIG. 3. Defect strength (d) as a function of misalignment in a sublattice point. Here $m_{\min} = 10^{-4}$ and $m_{\max} = 5 \times 10^{-3}$.

the facet middles with the central point as a square root of the multiple of the defect strengths of the central point and of the corresponding facet middle. In the end, the defect strength (probability of defect) in seven middle points (six facet middles and one cubic cell middle) and in six segments is determined. If the defect strength of some segment is different from zero, the linear defect along this segment is supposed. If the defect strengths of all segments in the cell are equal to zero, but at the same time, the defect strength of the corresponding center of the cell is different from zero, the point defect is supposed in the cell. Finally, we introduced the maximum value of $(\mathrm{div}\,\mathbf{n})^2$, above which the only point defect without linear defects is assumed in the cell regardless of the defect strengths of all segments.

An empirical algorithm described above does not incorporate the topological charge of defects and approximates the core energies of linear defects of all types with the same values, and the core energies of point defects of all types with another single value. However, in the absence of defects with sufficiently different absolute topological charge values the algorithm works appropriately, as shown in Sec. III.

We run this algorithm for each Monte Carlo step, so we update the positions and kinds of defects with any change of the director field. The energy of linear and point defects we use in our numerical scheme will be defined in the following paragraph.

5. *Defects energy*

When the defect strength in all six segments and the defect kind are defined for a particular cell, its defect energy F_{def} can be assigned. The energy of a point defect is calculated as

$$F_{\mathrm{def}} = F_{\mathrm{core}}^{\mathrm{point}}\, d_{cp},$$

where $F_{\mathrm{core}}^{\mathrm{point}}$ is the energy of a point defect core, which is an input parameter of the model as well as the elastic constants. The energy of a linear defect is calculated as

$$F_{\mathrm{def}} = \sum_{\alpha} f_{\mathrm{core}}^{\mathrm{line}}\, d_{\alpha}\, L_{\alpha}^{\mathrm{inside}},$$

where $f_{\mathrm{core}}^{\mathrm{line}}$ is the linear energy density of a linear defect core (which is also an input parameter) and $L_{\alpha}^{\mathrm{inside}}$ is part of the αth segments' length, which is inside of volume V.

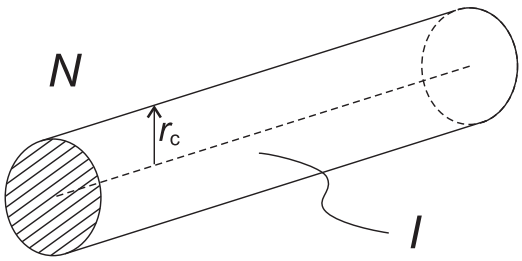

FIG. 4. A model of linear defect: cylindric isotropic core (I) and perfect nematic outside (N).

Following the approach introduced by Kleman and Lavrentovich [45], let us consider the linear defect core as a cylinder (Fig. 4) of radius r_c with isotropic phase inside, while the homogeneous nematic phase with order parameter S is distributed outside of cylinder r_c and inside of some larger cylinder of radius $r \gg r_c$. Defining the difference between free energy densities of nematic and isotropic states as f_c, one can estimate the total free energy inside of the r cylinder as follows:

$$F = l\left(\pi K k^2 \ln\frac{r}{r_c} + f_c \pi r_c^2\right),$$

where K is the elasticity constant in single constant approximation, k is the order of the defect, and l is the length of the cylinder. Minimizing free energy F with respect to r_c one obtains the energy-optimal radius of a defect core as $r_c = k\sqrt{\frac{K}{f_c}}$. Here we are going to consider the defect core radius as a maximum of r_c and correlation length.

One can estimate f_c from the Landau–de Gennes theory as in [20]:

$$f_c = \tfrac{3}{4}a\,(T - T_{NI}^{*})S^2 + \tfrac{1}{4}BS^3 + \tfrac{9}{16}CS^4,$$

where S is the order parameter of nematic phase. Substituting a, B, and C with typical values [20] of $10^5\,\mathrm{J\,m^{-3}\,K^{-1}}$, $-10^6\,\mathrm{J\,m^{-3}}$, and $10^6\,\mathrm{J\,m^{-3}}$, respectively, and assuming $S = 0.535$ [46] and $k = \frac{1}{2}$ one obtains $f_c \approx 2.74 \times 10^5\,\mathrm{J\,m^{-3}}$, and, as a result, $r_c \approx 2.5$ nm. Considering a correlation length of about 6.6 nm [47] (and then the core radius is also 6.6 nm instead of 2.5 nm), one obtains $f_{\mathrm{line}}^{\mathrm{core}} \approx 3.75 \times 10^{-11}\,\mathrm{J\,m^{-1}}$, or $f_{\mathrm{line}}^{\mathrm{core}}\,\mathrm{K}^{-1} \approx 6.1$.

C. Free energy minimization

As discussed above, we use MC simulated annealing [23] with Metropolis criterion [48] which does not require any preassumptions on director distribution. It can successfully start from a random state and converge to the global minimum. Results of a set of independent starts can be used to verify whether the annealing converges to the global minimum and not to some local minimum.

At each MC step, a random lattice point is selected. Then the director $\mathbf{n}$ in this point is changed randomly in correspondence with current MC temperature (T_{MC}): $\mathbf{n} \to \mathbf{n} + \Delta\mathbf{n}$, where the rms of the projections of $\Delta\mathbf{n}$ on all coordinate axes Δn_x, Δn_y, and Δn_z proportional to $\sigma\sqrt{k_B T_{\mathrm{MC}}}$ are generated with Box-Muller transformation [49]. Then the new director $\mathbf{n}$ is normalized. Here σ plays the role of a unit translation coefficient and also sets the value of the mean acceptance ratio

of MC steps. We chose σ accordingly to mean acceptance ratio close to 0.5.

The starting temperature $T_{\mathrm{MC}}^{\mathrm{start}}$ is set sufficiently large to reach the maximum possible free energy in the beginning of annealing. Thus, the system is guaranteed to be independent of initial state and therefore is optimized globally and not locally. For the systems studied below we are using $k_B T_{\mathrm{MC}}^{\mathrm{start}} = 2 \times 10^{-15}$ J $\approx 5 \times 10^5 k_B T$, which is empirically found to be reasonably large. The final temperature $T_{\mathrm{MC}}^{\mathrm{final}}$ determines the quality of optimization of the final state. We are using $k_B T_{\mathrm{MC}}^{\mathrm{final}} = 2 \times 10^{-22}$ J $\approx 5 \times 10^{-2} k_B T$, below which the director distribution does not change to any noticeable extent.

The MC temperature undergoes an exponential decay during the optimization steps. The amount of steps is defined by the lattice size as 10^4 steps per lattice point.

III. RESULTS AND DISCUSSION

In the present section we are going to present our numerical results obtained by the method described above. The structures discussed below can be obtained at typical values of the elasticity constants. In particular, we are using the values measured for 5CB at the temperature 10 K below nematic-isotropic transition from [50]: $K_{11} = 6.2 \times 10^{-12}$ N, $K_{22} = 3.9 \times 10^{-12}$ N, and $K_{33} = 9.8 \times 10^{-12}$ N, which are also in a good agreement with [46].

Theoretical approaches usually deal with spherical droplets for simplicity. In many experimental techniques, which are used for the creation of PDLC films, however, the droplets appear to be oblate. In the present paper we are going to apply our method to the oblate disklike droplets and to outline some new properties, which are not specific to the spherical droplets. Before that, however, we are going to verify several structures obtained previously in spherical droplets by different methods.

A. Electric-field-induced transitions in spherical nematic droplets with homeotropic anchoring

1. Equilibrium structures

We applied the method described above to the spherical supramicrometer nematic droplets with homeotropic surface conditions. Let us introduce the dimensionless anchoring strength $\mu = \frac{WR}{K_{11}}$ varying from 10 to 2000 and the dimensionless uniform electric field $e = ER(\frac{\varepsilon_0 \Delta\varepsilon}{K_{11}})^{1/2}$ varying from zero to 150, where R is the droplet radius. To obtain the equilibrium structures of a droplet at particular values of μ and e, we have done Monte Carlo optimization in eight independent runs per each μ and e, and then the structure with the lowest free energy was selected as the equilibrium structure. Totally we have found the three equilibrium structures of a spherical droplet, which are presented in the phase diagram in Fig. 5.

(1) Radial structure (R, marked with black squares in Fig. 5), or hedgehoglike structure, in which only one point defect exists in the center of the droplet. This structure arises when the surface energy dominates over the elasticity energy and/or the electric-field energy.

(2) Axial structure without defects (A, marked with blue triangles in Fig. 5). This structure arises in the case, when the elasticity energy and/or the electric-field energy dominates over the surface anchoring energy.

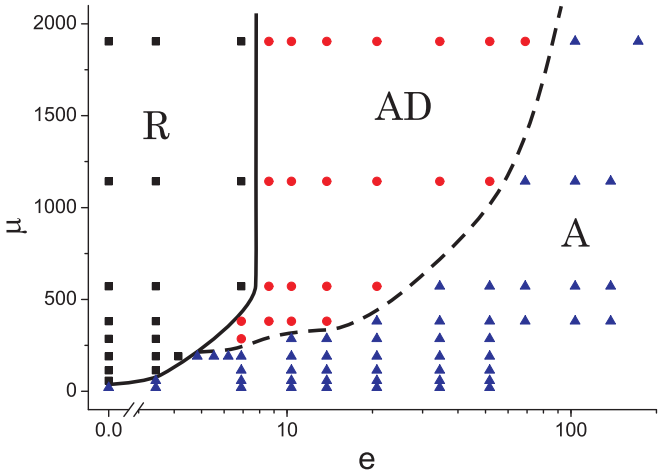

FIG. 5. (Color online) Diagram of states of 5CB nematic LC in spherical droplet with homeotropic anchoring under electric field. Here e denotes the dimensionless electric-field strength and μ denotes the dimensionless anchoring strength. Radial (R), axial (A) and axial with linear defect (AD) states are present.

(3) Axial structure with line defect (AD, marked with red circles in Fig. 5), which arises in between the axial and radial structures at strong enough surface anchoring under moderate electric field.

These structures and the phase diagram are in good agreement with those obtained by Kralj and Zumer [51]. A quantitative comparison of our results with Kralj and Zumers' data is presented below together with an analysis of all possible phase transitions (R-A, R-AD, and AD-A).

2. Direct transition between axial and radial structures (A-R transition)

The direct transitions between axial and radial structures can be observed, when the electric field increases at small anchoring strength or when the anchoring strength increases at small electric field (see left bottom corner of the diagram presented in Fig. 5). The qualitative behavior of the structure at the phase transition can be easily understood if one introduces the tensor order parameter $Q_{\alpha\beta} = \langle \frac{1}{2}(3 n_\alpha n_\beta - \delta_{\alpha\beta}) \rangle$, where n_α and n_β are the projections of local director $\mathbf{n}$ on coordinate axes α and β, and $\delta_{\alpha\beta}$ is the Kronecker symbol. Here the angular brackets denote the average over the whole droplet. One notes, that the order parameter $Q_{\alpha\beta}$ is introduced in the same manner as the nematic order parameter with the only difference that the local director participates instead of the molecular long axis, and the average is over a larger scale, at which the director itself exhibits considerable modification. In particular, in the homogeneous nematic state with the director along the z coordinate the diagonal elements of $Q_{\alpha\beta}$ should be equal to $-1/2$, $-1/2$, and 1, while at perfect radial distribution of the director inside a spherical droplet all the diagonal elements should be equal to zero. The nondiagonal elements should be equal to zero for any distribution of the director possessing the axial symmetry with respect to any coordinate axis; in particular, they should be equal to zero for both homogeneous

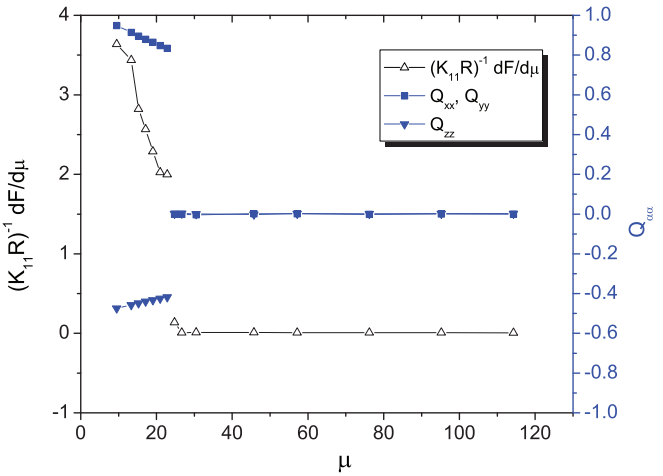

FIG. 6. (Color online) Dependencies of the dimensionless total free energy derivative $\frac{1}{K_{11}R}\frac{\partial F}{\partial \mu}$ and the diagonal elements of tensor order parameter $Q_{\alpha\beta}$ on the dimensionless surface anchoring strength μ in a spherical droplet with 5CB without electric field ($e = 0$). The first order phase transition from axial state (A) to radial state (R) happens at $\mu \approx 24 \pm 1$.

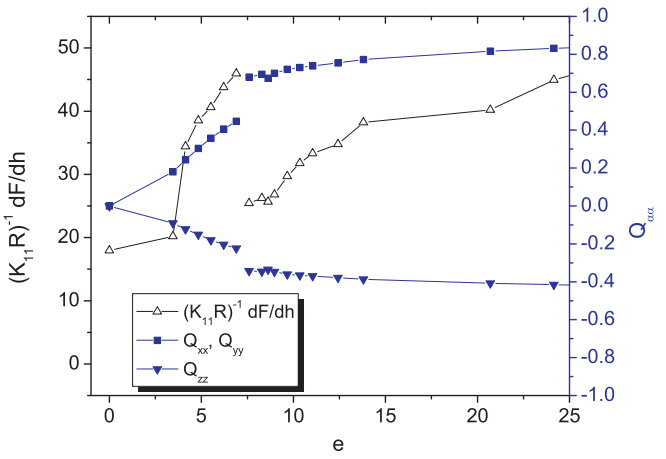

FIG. 7. (Color online) Dependencies of the dimensionless total free energy derivative $\frac{1}{K_{11}R}\frac{\partial F}{\partial h}$ and diagonal elements of tensor $Q_{\alpha\beta}$ on the dimensionless electric-field strength e in a spherical droplet with 5CB at strong surface anchoring ($\mu = 1100$). The first order phase transition from radial state (R) to axial state with linear defect (AD) happens at $e \approx 7.3 \pm 0.3$.

and axial distributions of the director inside of a spherical droplet considered above.

The dependence of calculated total free energy derivative in dimensionless form $\frac{1}{K_{11}R}\frac{\partial F}{\partial \mu}$ on the value of anchoring strength μ at zero electric field is presented in Fig. 6, as well as the dependence of the diagonal elements of tensor order parameter $Q_{\alpha\beta}$. The derivative changes stepwise at $\mu_{A-R} = 24 \pm 1$ indicating the first order phase transition. One notes that orientation of the director along a particular z axis dominates in the axial state, while in the radial state there is no domination of any particular orientation of the director. The anchoring strength at the transition point is in good agreement with [51].

3. *Axial structure with defect (AD)*

There is a critical point in the phase diagram ($\mu_c \approx 280$, $e_c \approx 4$), above which the axial structure with defect (AD) arises between the axial and radial structures (see Fig. 5). This result is again in good agreement with Ref. [51], where it was shown that the defect should arise in the plane perpendicular to the electric field at an anchoring strength larger than $\mu_c \approx 240$ in the single elasticity constant approximation. The dependencies of calculated dimensionless total free energy derivative $\frac{1}{K_{11}R}\frac{\partial F}{\partial h}$ on the value of electric field e at $\mu = 1100$ and the diagonal elements of tensor order parameter $Q_{\alpha\beta}$ are presented in Fig. 7. Both derivative and order parameter change stepwise at $e = 7.3 \pm 0.3$ indicating the first order phase transition.

Further increase of the electric-field strength leads to an increase of the defect ring. Finally the defect ring reaches the radius of a droplet, and one would expect the second order phase transition into the axial structure without defect. In our approach, however, which does not predetermine the axial symmetry of the structure, we see a different scenario. The defect ring breaks into pieces first, and then the length of each piece decreases. At present we cannot answer the question, whether this scenario is solely due to the approach we are using or not. The dependencies of the dimensionless defect energy, its derivative with respect to the electric field and the diagonal elements of tensor $Q_{\alpha\beta}$ on the electric-field strength are presented in Fig. 8. Both defect energy and order parameter vary rather continuously. Since our method cannot classify this structural change as a phase transition, we have plotted the dashed line in the phase diagram (Fig. 5) at a position corresponding to the maximum value of $|\frac{dF_{\rm def}}{dh}|$.

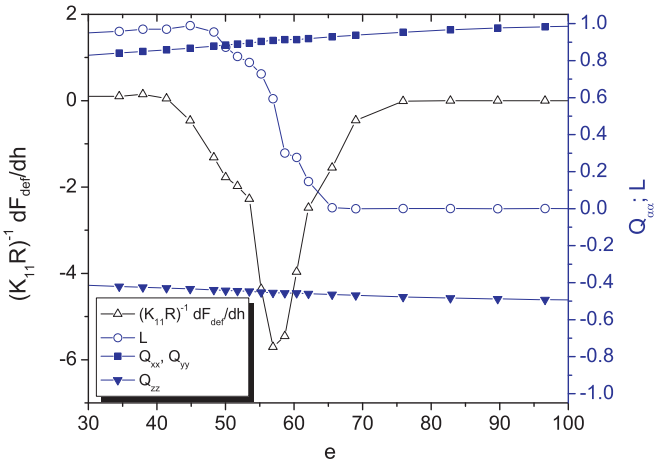

FIG. 8. (Color online) Dependencies of the dimensionless defect energy derivative $\frac{1}{K_{11}R}\frac{\partial F_{\rm def}}{\partial e}$ (black empty triangles), dimensionless length of defect $L = \frac{l}{2\pi R}$, where l is real length (blue empty circles), and diagonal elements of tensor $Q_{\alpha\beta}$ (blue filled squares and triangles) on the dimensionless electric-field strength e in a spherical droplet with 5CB at strong surface anchoring ($\mu = 1100$). The continuous transformation from axial state with linear defect (AD) to axial state (A) is observed.

B. Electric-field-induced transitions in the oblate nematic droplet with homeotropic anchoring

1. Equilibrium structures

Let us consider oblate ellipsoidal droplets with two long eigenvectors d_x and d_y, which are equal to each other, and one short eigenvector d_z. Let us introduce the degree of oblateness $\delta = \frac{d_x}{d_z}$ at a given volume of the droplet, which is greater or equal to one. Here we are going to use the same elasticity constants, as in the case of the spherical droplets, corresponding to the material 5CB (see above). We also suppose the strong homeotropic anchoring ($\mu = 2000$). For the oblate droplet, let one use mean size of the droplet R equal to radius of sphere with the same volume. The drastic difference from spherical droplets can be seen already without electric field, when the following two states can be observed at various oblateness δ [see Figs. 9(a)–9(c)]:

(1) Radial structure (R), or hedgehoglike structure, which arises at $\delta < 3.125$. The director deformation gradually increases with the increasing oblateness [see Figs. 9(a)–9(c)], while the defect topology remains the same (only one point defect exists in the center of a droplet).

(2) Axial structure with the line defect (AD) arises at $\delta > 3.125$. At strong oblateness the circular defect line of diameter close to d_x arises, as shown in Fig. 9(d). The almost uniform director distribution is observed in the inner part of the droplet (inside of the defect ring), while the outer part of the structure appears to be strongly deformed. One can see that, in contrast to the case of spherical droplets, the AD structure arises without electric field solely due to the homeotropic anchoring at the surface.

When the electric field is applied along the short axis (the symmetry axis) of the droplet, the sequence of states depending on the droplet oblateness δ is quite simple. At $\delta < 3.125$, the sequence of states is R $\rightarrow$ AD $\rightarrow$ A, the same as for the spherical droplet. At $\delta > 3.125$, the AD state exists at no field instead of R state, and the sequence of states is then AD $\rightarrow$ A. The corresponding oblateness–electric-field phase diagram is shown in Fig. 10, where R is marked with black squares, AD is marked with red circles, and A is marked with green up triangles. The thresholds of both transitions decrease with the increasing δ, but the transition kinds remain the same as for the spherical droplet.

It is more interesting to consider the case when the electric field is applied along one of the long axes of the droplet (perpendicular to the symmetry axis of the droplet). The phase diagram appears to be richer in this case, since the symmetry of the system is broken. Our simulations reveal the following states:

(1) Radial structure (R), described above [see Figs. 9(a)–9(c)].

(2) Axial structure with defect (AD), described above [see Figs. 9(d) and 11(a)].

(3) Asymmetric structure with tilted director distribution in the central part of the droplet (TD), where the director tends to be oriented along the electric field. The circular defect line exists at approximately the same position as in the previous case. The structure is shown in Fig. 11(b). This structure arises at $\delta > 3.125$ in the presence of a small electric field.

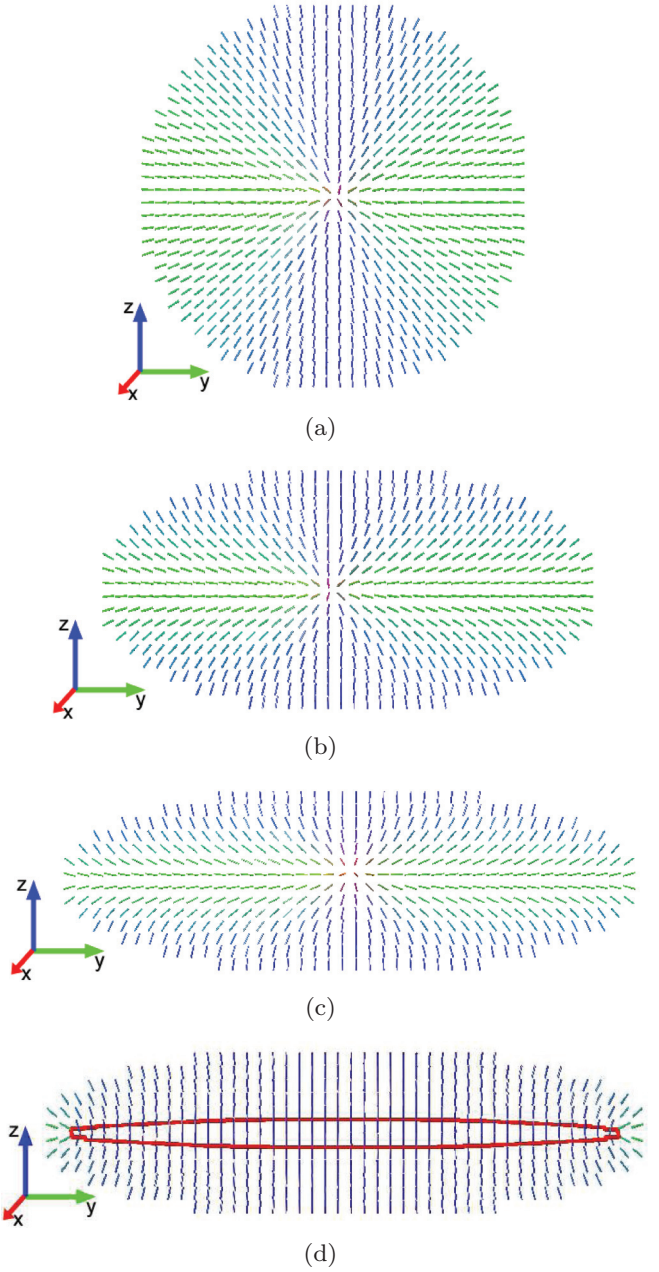

FIG. 9. (Color online) Structures of 5CB in droplets with strong homeotropic anchoring ($\mu = 2000$) and various oblateness: $\delta = 0$ (a), $\delta = 2$ (b), $\delta = 3$ (c), and $\delta = 3.5$ (d). Director vectors are colored in correspondence with their direction orientation. Defect is marked with a bold red line.

(4) Asymmetric structure with tilted director distribution and also with tilted defect ring (TTD) [see the structure in Fig. 11(c)]. It arises at any oblateness δ in the presence of an electric field high enough to suppress the elasticity energy of the liquid crystal. The defect ring tilts gradually with the increasing electric field and becomes almost perpendicular to the electric-field direction when h tends to infinity [see Figs. 11(c) and 11(d)]. The limit orientation of the defect ring in the TTD structure is the same as that for the AD structure in the spherical droplet.

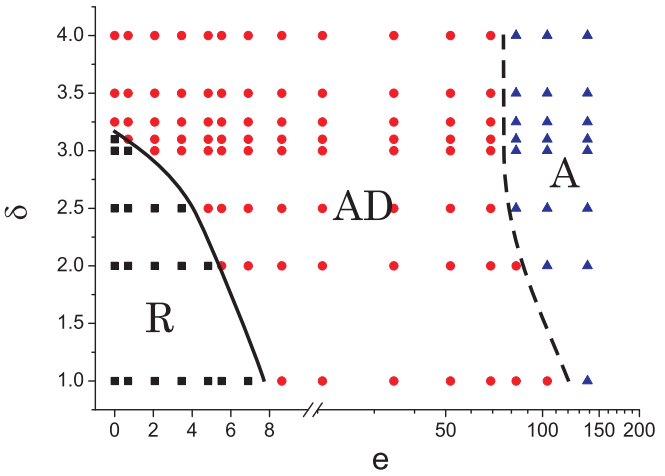

FIG. 10. (Color online) Diagram of states of 5CB nematic LC in an oblate droplet with homeotropic anchoring ($\mu = 2000$) under electric field applied along the short axis of the droplet. Here e denotes the reduced electric-field strength, and δ denotes the oblateness of a droplet. The solid line denotes the phase transition border between the R and AD states, and the dashed line denotes the maximum transformation between the AD and A states.

(5) Axial structure without defects (A). This structure arises when the electric field is high enough to suppress the surface boundaries [see Fig. 11(e)].

The corresponding oblateness–electric-field phase diagram is shown in Fig. 12, where R is marked with black squares, AD is marked with purple down triangles, TD is marked with green rhombuses, TTD is marked with red circles, and A is marked with blue up triangles.

The mechanisms of R → TTD and TTD → A transitions are the same as that for R → AD and AD → A observed in spherical droplets (see details in the previous section). The transitions R → AD, AD → TD, and TD → TTD are specific to oblate droplets only, and their details will be described below.

2. *Transition from radial structure to axial structure with defect (R-AD transition)*

The radial structure arises in a spherical droplet at an appropriate balance between homeotropic surface anchoring and elasticity energy [see Fig. 9(a)]. In a slightly oblate droplet [see Figs. 9(b) and 9(c)] the deformed radial structure arises with maximum deformation near the plane containing the two long eigenvectors, and increasing when δ increases. Above some critical value of oblateness, the transition to the axial structure with linear defect happens. The defect ring is then located in the same plane located near the surface. The structure inside of the defect ring appears to be almost uniform, while the outer part appears to be strongly deformed [see Fig. 9(d)]. The elasticity energy of the droplet in this structure is smaller than in the AD structure and is compensated by the defect energy. Both the first derivative of the dimensionless free energy $\frac{1}{K_{11}R}\frac{\partial F}{\partial \delta}$ and the order parameter $Q_{\alpha\beta}$ change stepwise at critical oblateness $\delta_{R\to AD} = 3.125 \pm 0.025$ (see Fig. 13)

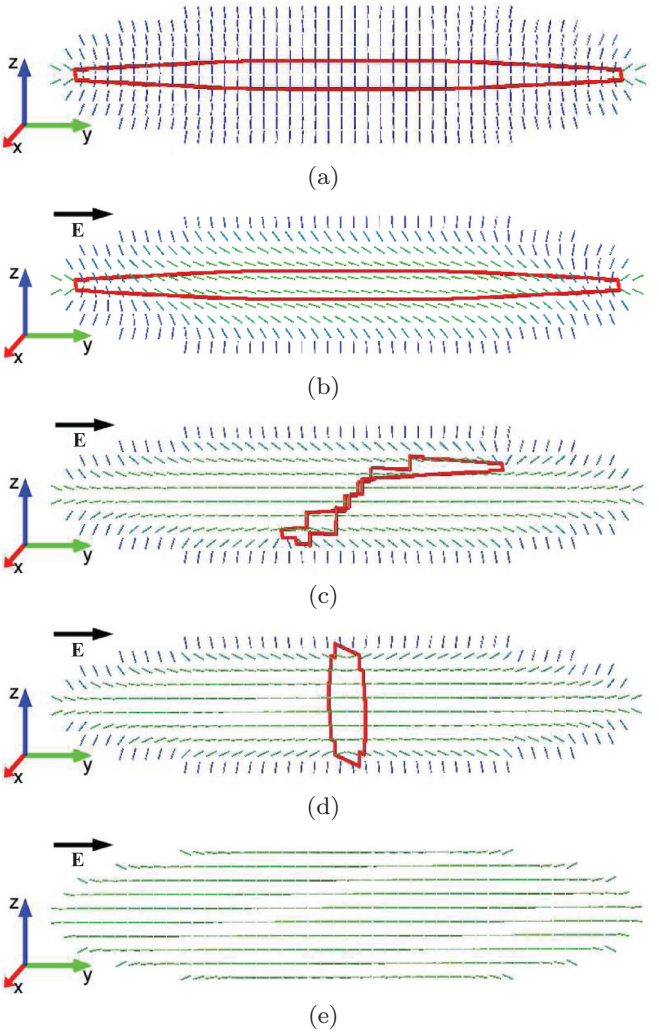

FIG. 11. (Color online) Structures of 5CB in a droplet of oblateness $\delta = 4$ with strong homeotropic anchoring ($\mu = 2000$) and various electric-field strengths: axial state with linear defect (AD) at $e = 0$ (a), tilted state with defect (TD) at $e = 4.0$ (b), tilted state with tilted defect (TTD) at $e = 5.0$ (c), TTD state at $e = 52.5$ (d), and axial state (A) at $e = 103.5$ (e). Director vectors are colored in correspondence with their direction orientation. Defect is marked with a bold red line.

indicating the first order phase transition shown with a solid black line in Fig. 12.

3. *Transition from axial structure with defect to tilted structure with defect (AD-TD transition)*

This transition occurs at $\delta > \delta_{R\to AD}$ at moderate values of electric field. Below the critical value of the electric field $e < e_{AD\to TD}$, the director distribution is approximately the same as at $e = 0$ [see Fig. 11(a)]. At $e_{AD\to TD} = 3.6 \pm 0.1$ the transition to the tilted director structure with the same position of defect occurs [see Fig. 11(b)]. We have analyzed the details of this transition by calculation of the free energy derivatives and order parameter as functions of e [Fig. 14]. The linear approximations to the first derivative of the dimensionless free energy in the ranges of electric field below and above $e_{AD\to TD}$

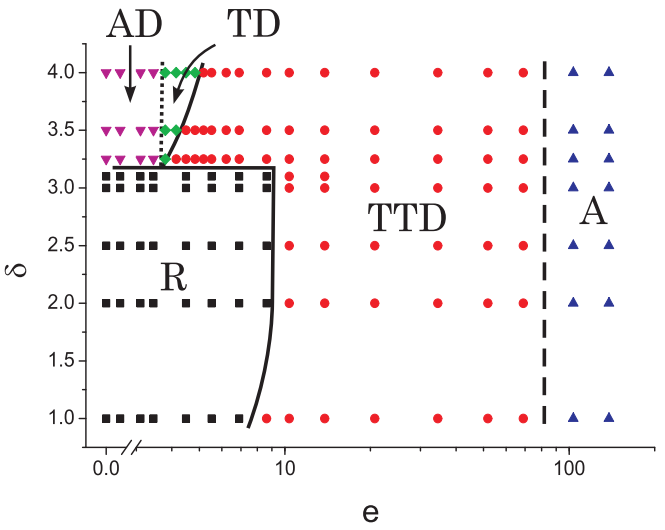

FIG. 12. (Color online) Diagram of states of 5CB nematic LC in an oblate droplet with homeotropic anchoring ($\mu = 2000$) under an electric field applied along the long axis of the droplet. Here e denotes the dimensionless electric-field strength and δ denotes the oblateness of a droplet. Radial (R), axial (A), axial with linear defect (AD), tilted structure with defect (TD), and tilted structure with tilted defect (TTD) are present. Solid lines correspond to the first order phase transitions, the dotted line corresponds to the second order phase transition, and the dashed line corresponds to the strongest continuous transformation from TTD to A.

are shown with red lines in Fig. 14. Intersection of these two lines shows the approximate transition point. The same point can be found from direct calculations of the second derivative $\frac{1}{K_{11}R}\frac{\partial^2 F}{\partial e^2}$ (plotted with black empty circles in Fig. 14). It has a stepwise change at $e_{\mathrm{AD}\to\mathrm{TD}}$. Order parameter (blue rhombus in Fig. 14) remains almost constant below the critical field $e_{\mathrm{AD}\to\mathrm{TD}}$, and changes gradually above this point. Behavior of both the second derivative of free energy and the order parameter indicates the second order phase transition shown in the phase diagram (Fig. 12) with a dotted line.

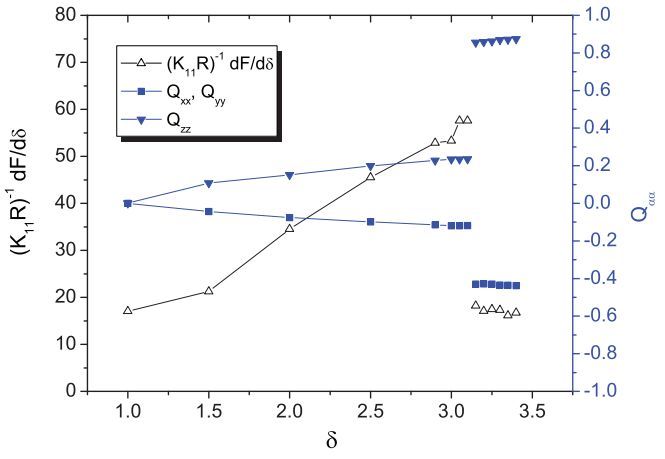

FIG. 13. (Color online) Dependencies of dimensionless total free energy derivative $\frac{1}{K_{11}R}\frac{\partial F}{\partial \delta}$ and diagonal elements of tensor $Q_{\alpha\beta}$ on oblateness δ of a droplet with 5CB, no electric field. First order phase transition at $\delta_{\mathrm{R}\to\mathrm{AD}} = 3.125 \pm 0.025$.

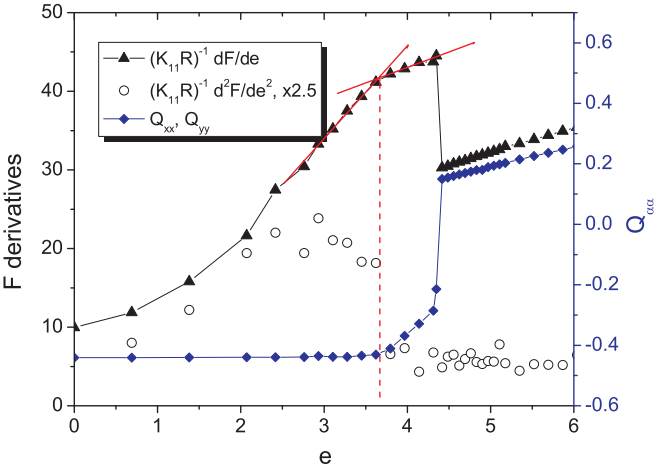

FIG. 14. (Color online) Dependencies of first and second derivatives of dimensionless total free energy ($\frac{1}{K_{11}R}\frac{\partial F}{\partial e}$ and $\frac{1}{K_{11}R}\frac{\partial^2 F}{\partial e^2}$, shown in black triangles with black line and black circles, consequently), and order parameter Q_{yy} (blue rhombus) on reduced electric-field strength e for 5CB in oblate droplet ($\delta = 3.5$). Strong surface anchoring ($\mu = 2000$). Red solid lines show linear approximations to $\frac{1}{K_{11}R}\frac{\partial F}{\partial e}$ in regions near second order phase transition AD $\to$ TD ($e_{\mathrm{AD}\to\mathrm{TD}} = 3.6 \pm 0.1$). First order phase transition TD $\to$ TTD occurs at $e_{\mathrm{TD}\to\mathrm{TTD}} = 4.38 \pm 0.04$.

4. Transition from tilted structure with nontilted defect to tilted structure with tilted defect (TD-TTD transition)

At some larger critical value of the electric field $e_{\mathrm{TD}\to\mathrm{TTD}}$ at oblateness $\delta > \delta_{\mathrm{R}\to\mathrm{AD}}$ the first order transition to a different structure happens, where the defect line also appears to be tilted. Below $e_{\mathrm{TD}\to\mathrm{TTD}}$ only the director tilt in the central part of the droplet increases with the increasing electric field, while the location of the defect line remains unchanged. Above $e_{\mathrm{TD}\to\mathrm{TTD}}$ the defect line rotates stepwise by angle about 30° around the long eigenvector of ellipsoid, which is perpendicular to the electric-field direction [see Fig. 11(c)]. This transition reduces the elasticity energy competing with the electric-field energy. Figure 14 shows that the transition point is very close to AD $\to$ TD transition (for example, $e_{\mathrm{TD}\to\mathrm{TTD}} = 4.38 \pm 0.04$ for $\delta = 3.5$). The difference between two critical values of the electric field, $e_{\mathrm{AD}\to\mathrm{TD}}$ and $e_{\mathrm{TD}\to\mathrm{TTD}}$, grows with the increasing oblateness δ, while near the critical oblateness $\delta_{\mathrm{R}\to\mathrm{AD}}$ both transitions tend to coincide with each other.

IV. CONCLUSIONS

In the present paper a method for fast director distribution calculations in liquid crystal droplets in the framework of elastic continuum theory is presented. The theoretical approach is expanded with point and linear disclinations, which are explicitly taken into account in the numerical scheme. The expansion uses the empirical approach, which does not take into consideration detailed information about the defects, such as topological charge or core structure of the defect [18,19,52]. This method uses Monte Carlo simulated annealing for global energy optimization. A special triangulation technique is suggested for representing the boundaries, which allows one to predict the director distribution in a droplet of any shape. The recent version of the software can be found on the link [53].

First we have shown that our method gives the correct results for the case of spherical nematic droplet in the electric field, where the director distribution can be either calculated with more complex methods, or verified experimentally. Despite a very simple representation of the defects, the suggested method works fine, when only topological defects of the same topological charge are presented in the system. In particular, we obtained the radial, axial without defects, and axial with circular defect structures, and the corresponding phase diagram is very similar to the one predicted earlier in [51].

Using our method we investigated various nematic structures arising in the oblate droplets, which are normally created during PDLC preparation techniques. It was demonstrated that strongly oblate droplets tend to have large circular defect even without electric field. This fact gives rise to the existence of several new structures in the electric field applied perpendicular to the principal (short) axis of the oblate droplet. In particular, we recognized the new tilted structure with circular defect lying in the longitudinal plane of the oblate ellipsoid (TD) and tilted structure, where the circular defect is also tilted with respect to the longitudinal plane of the oblate ellipsoid (TTD). These are two intermediate structures between the two axial structures, the one existing without electric field (or at small electric field) with the director tending to be oriented along the short eigenvector of the oblate ellipsoid, and another one arising at large electric field with the director tending to be oriented along the long eigenvector of the oblate ellipsoid, which is collinear to the electric-field direction.

PDLC materials consisting of spherical (or weakly oblate) droplets usually demonstrate the nontransparent R state without electric field and the transparent AD state in the electric field. In contrast, PDLC materials consisting of strongly oblate droplets should demonstrate transparent AD state without electric field and nontransparent TD state at small electric field. Our calculations suggest that the transition between AD and TD states in strongly oblate droplets should happen at approximately twice smaller electric field than the transition between R and AD states in spherical droplets at the same anchoring strength. Thus, our investigations suggest that PDLC materials consisting of strongly oblate droplets can be used for creation of the low-voltage optical devices.

PDLC materials consisting of strongly oblate droplets can also be used for creation of high-contrast optical devices based on birefringence (using polarizers). Indeed, the apparent birefringence should arise in one of the two axial states, and should disappear in another one. The existence of two intermediate states (TD and TTD) can also be used for creation of several birefringence colors at different voltages [54].

Thus, in the present paper we have outlined several new structures and several new capacities of PDLC materials composed of strongly oblate droplets. The optical properties of the structures reported here should, however, be accurately investigated in a separate publication.

ACKNOWLEDGMENTS

We gratefully acknowledge the support of Russian Ministry of Education and Science (Project No. MD-4909.2014.2) and Russian Foundation for Basic Research (Projects No. 12-03-90021, No. 14-02-92017, and No. 14-02-92105). All the calculations were performed on “Lomonosov” supercomputer in M. V. Lomonosov Moscow State University.

[1] *Handbook of Liquid Crystals*, edited by D. Demus, J. Goodby, G. Gray, H. Spiess, and V. Vill (Wiley-VCH Verlag GmbH, Weinheim, 1998).
[2] G. Montgomery, C. Smith, and N. Vaz, *Liquid Crystalline and Mesomorphic Polymers* (Springer-Verlag, New York, 1995).
[3] *Liquid Crystals in Complex Geometries*, edited by G. Crawford and S. Žumer (Taylor & Francis, London, 1996).
[4] A. S. Sonin and N. A. Churochkina, Polym. Sci., Ser. A **52**, 463 (2010).
[5] J. Guo, H. Yang, R. Li, N. Ji, X. Dong, H. Wu, and J. Wei, J. Phys. Chem. C **113**, 16538 (2009).
[6] F. Bloisi and L. Vicari, *Optical Application of Liquid Crystals* (Taylor & Francis, London, 2003).
[7] V. A. Loiko, A. V. Konkolovich, and P. G. Maksimenko, J. Soc. Inf. Disp. **14**, 595 (2006).
[8] V. A. Loiko, A. V. Konkolovich, and A. A. Miskevich, J. Exp. Theor. Phys. **105**, 846 (2007).
[9] D.-K. Yang, J. L. West, L.-C. Chien, and J. W. Doane, J. Appl. Phys. **76**, 1331 (1994).
[10] K. Chari, C. M. Rankin, D. M. Johnson, T. N. Blanton, and R. G. Capurso, Appl. Phys. Lett. **88**, 043502 (2006).
[11] A. V. Emelyanenko, M. A. Osipov, and D. A. Dunmur, Phys. Rev. E **62**, 2340 (2000).
[12] A. V. Emelyanenko, Phys. Rev. E **67**, 031704 (2003).
[13] V. Y. Zyryanov, M. N. Krakhalev, O. O. Prishchepa, and A. V. Shabanov, JETP Lett. **86**, 383 (2007).
[14] P. Lebwohl and G. Lasher, Phys. Rev. A **6**, 426 (1972).
[15] I.-An Yao, Y.-C. Lai, S.-H. Chen, and J.-J. Wu, Phys. Rev. E **70**, 051705 (2004).
[16] I.-A. Yao, J.-J. Wu, and S.-H. Chen, Jpn. J. Appl. Phys. **43**, 1488 (2004).
[17] S. Kralj, E. G. Virga, and S. Zumer, Phys. Rev. E **60**, 1858 (1999).
[18] D. Svensek and S. Zumer, Phys. Rev. E **70**, 040701 (2004).
[19] M. Svetec, S. Kralj, Z. Bradac, and S. Zumer, Eur. Phys. J. E **20**, 71 (2006).
[20] M. Ravnik and S. Žumer, Liq. Cryst. **36**, 1201 (2009).
[21] M. Ravnik and S. Zumer, Soft Matter **5**, 269 (2009).
[22] F. C. Frank, Discuss. Faraday Soc. **25**, 19 (1958).
[23] S. Kirkpatrick, Jr., C. D. Gelatt, and M. P. Vecchi, Science **220**, 671 (1983).
[24] C. C. Bowley, A. K. Fontecchio, G. P. Crawford, J.-J. Lin, L. Li, and S. Faris, Appl. Phys. Lett. **76**, 523 (2000).
[25] I. Shiyanovskaya, S. Green, A. Khan, G. Magyar, O. Pishnyak, and J. W. Doane, J. Soc. Inf. Disp. **16**, 113 (2008).

[26] K. Lv, D. Liu, W. Li, Q. Tian, and X. Zhou, Dyes Pigm. **94**, 452 (2012).
[27] H. H. Liang, C. C. Wu, P. H. Wang, and J. Y. Lee, Opt. Mater. **33**, 1195 (2011).
[28] Q. Li, Y. Li, J. Ma, D. K. Yang, T. J. White, and T. J. Bunning, Adv. Mater. **23**, 5069 (2011).
[29] L. H. Domash, Y.-M. Chen, B. Gomatam, C. Gozewski, R. L. Sutherland, L. V. Natarajan, V. P. Tondiglia, T. J. Bunning, and W. W. Adams, Proc. SPIE **2689**, 188 (1996).
[30] M. Popovich and S. Sagan, SID Digest of Tech. Pap. **31**, 1060 (2000).
[31] T. G. Fiske, L. D. Silverstein, J. Colegrove, and H. Yuan, SID Digest of Tech. Pap. **31**, 1134 (2000).
[32] E. Enz and J. Lagerwall, J. Mater. Chem. **20**, 6866 (2010).
[33] T. Manabe, K. Sonoyama, Y. Takanishi, K. Ishikawa, and H. Takezoe, J. Mater. Chem. **18**, 3040 (2008).
[34] N. P. N. Huck, I. Staupe, A. Thirouard, and D. K. G. Deboer, Jpn. J. Appl. Phys. **42**, 5189 (2003).
[35] C. Chiccoli, P. Pasini, F. Semeria, E. Berggren, and C. Zannoni, Mol. Cryst. Liq. Cryst. **266**, 241 (1995).
[36] E. Berggren, C. Zannoni, C. Chiccoli, P. Pasini, and F. Semeria, Phys. Rev. E **49**, 614 (1994).
[37] C. Chiccoli, P. Pasini, F. Semeria, and C. Zannoni, Phys. Lett. A **150**, 311 (1990).
[38] B.-G. Wu, J. H. Erdmann, and J. W. Doane, Liq. Cryst. **5**, 1453 (1989).
[39] R. K. Bharadwaj, T. J. Bunning, and B. L. Farmer, Liq. Cryst. **27**, 591 (2000).
[40] R. H. J. Otten and P. van der Schoot, J. Chem. Phys. **137**, 154901 (2012).
[41] M. Jazbinsek, D. Olenik, M. Zgonik, A. K. Fontecchio, and G. P. Crawford, J. Appl. Phys. **90**, 3831 (2001).
[42] M. de Berg, M. van Kreveld, M. Overmans, and O. Schwarzkopf, *Computational Geometry: Algorithms and Applications*, 2nd ed. (Springer-Verlag, Berlin, 2000).
[43] A. Rapini and M. J. Papoular, J. Phys. Colloq. **30**, C4 (1969).
[44] P. G. de Gennes and J. Prost, *The Physics of Liquid Crystals*, 2nd ed. (Claerendon Press, Oxford, 1993).
[45] M. Kleman and O. Lavrentovich, *Soft Matter Physics: An Introduction* (Springer, New York, 2002).
[46] N. V. Madhusudana and R. Pratibha, Mol. Cryst. Liq. Cryst. **331**, 49 (1999).
[47] M. Ravnik, B. Crnko, and S. Zumer, Mol. Cryst. Liq. Cryst. **208**, 150 (2009).
[48] I. Beichl and F. Sullivan, Comput. Sci. Eng **2**, 65 (2000).
[49] G. E. P. Box and M. E. Muller, Ann. Math. Stat. **29**, 610 (1958).
[50] G.-P. Chen, H. Takezoe, and A. Fukuda, Liq. Cryst. **5**, 341 (1989).
[51] S. Kralj and S. Zumer, Phys. Rev. A **45**, 2461 (1992).
[52] Z. Bradac, S. Kralj and S. Zumer, Phys. Rev. E **58**, 7447 (1998).
[53] V. Y. Rudyak, *LCOptimizer software package* 2013, URL http://polly.phys.msu.ru/ru/labs/lc/research-lcoptimizer-en.html.
[54] A. V. Emelyanenko, E. P. Pozhidaev, N. M. Shtykov, and V. E. Molkin, J. Soc. Inf. Disp. **8**, 16 (2008).